Soft Matter

Soft Matter

ARTICLE TYPE

Using Delaunay triangularization to characterize non-affine displacement fields during athermal, quasistatic deformation of amorphous solids[†]

Weiwei Jin,[a] Amit Datye,[a] Udo D. Schwarz,[ab] Mark D. Shattuck,[c] and Corey S. O'Hern[*adef]

We investigate the non-affine displacement fields that occur in two-dimensional Lennard-Jones models of metallic glasses subjected to athermal, quasistatic simple shear (AQS). During AQS, the shear stress versus strain displays continuous quasi-elastic segments punctuated by rapid drops in shear stress, which correspond to atomic rearrangement events. We capture all information concerning the atomic motion during the quasi-elastic segments and shear stress drops by performing Delaunay triangularizations and tracking the deformation gradient tensor F_α associated with each triangle α. To understand the spatio-temporal evolution of the displacement fields during shear stress drops, we calculate F_α along minimal energy paths from the mechanically stable configuration immediately before to that after the stress drop. We find that quadrupolar displacement fields form and dissipate both during the quasi-elastic segments and shear stress drops. We then perform local perturbations (rotation, dilation, simple and pure shear) to single triangles and measure the resulting displacement fields. We find that local pure shear deformations of single triangles give rise to mostly quadrupolar displacement fields, and thus pure shear strain is the primary type of local strain that is activated by bulk, athermal quasistatic simple shear. Other local perturbations, e.g. rotations, dilations, and simple shear of single triangles, give rise to vortex-like and dipolar displacement fields that are not frequently activated by bulk AQS. These results provide fundamental insights into the non-affine atomic motion that occurs in driven, glassy materials.

1 Introduction

The mechanical response of amorphous solids, such as colloidal and metallic glasses, is extremely complex. For example, during shear, compression, and other bulk mechanical tests, amorphous solids display collective spatio-temporal dynamics including stress localization, shear banding, and fracture.[1–6] In crystalline solids, the motion of atoms near topological defects (such as point defects, dislocations, and grain boundaries) and the interaction between these defects control the mechanical response

of the system.[7] However, it has been difficult to identify the structural "defects" that determine the mechanical response in amorphous solids.[8]

Early work by Argon,[9] and extensive further studies by Falk and Langer,[10] have emphasized the importance of shear transformation zones (STZs), which are clusters of atoms (or particles) that move cooperatively with much larger displacements than the surrounding atoms, in amorphous solids undergoing applied deformations. Subsequent studies have attempted to characterize the size, shape, activation, and evolution of STZs in amorphous solids during applied deformation.[4,8,11–18]

There are numerous open questions concerning the definition and interpretation of STZs in amorphous solids. First, are STZs the structural "defects" that control mechanical response in amorphous solids, similar to topological defects in crystalline solids, or are STZs the atomic flow fields that result from yet undetected structural defects? The majority of recent studies argue for the former case, i.e., STZs should be classified as the fundamental defects that control the mechanical response of amorphous solids.[13,19–30]

During quasistatic loading, the stress response of amorphous

[a] Department of Mechanical Engineering and Materials Science, Yale University, New Haven, Connecticut 06520, USA

[b] Department of Chemical and Environmental Engineering, Yale University, New Haven, Connecticut 06520, USA

[c] Benjamin Levich Institute and Physics Department, The City College of New York, New York, New York 10031, USA

[d] Department of Physics, Yale University, New Haven, Connecticut 06520, USA

[e] Department of Applied Physics, Yale University, New Haven, Connecticut 06520, USA

[f] Graduate Program in Computational Biology and Bioinformatics, Yale University, New Haven, Connecticut 06520, USA. E-mail: corey.ohern@yale.edu

solids first shows elastic behavior for small strains, followed by sudden drops in stress caused by atomic rearrangement events. This behavior is repeated, i.e., smooth quasi-elastic increases in stress followed by rapid stress drops, with further increases in strain. Non-affine collective atomic displacements can occur in the quasi-elastic regions, but the non-affine motion is much larger during the stress drops and it has been extremely difficult to predict at what strains the stress drops occur and the resulting non-affine atomic motion.[19,20,24–26,28,29] Several groups have attempted to predict "soft spots" in amorphous solids, i.e., regions of large non-affine displacements resulting from mechanical instabilities that occur during athermal quasistatic shear.[24,27,31,34] Methods that incorporate higher-order spatial derivatives of the dynamical matrix can predict soft spots further from the instability than first-order methods,[24,26,31,34] but the accuracy of these methods is limited by the magnitude of the stress drop. To gain further insight into the non-affine displacement fields resulting from large stress drops, in this article, we follow the evolution of the system along minimal energy paths as it evolves from the mechanically stable state before to that after the instability.

In this article, we address several important, open questions concerning the mechanical response of amorphous solids by developing a novel methodology for characterizing non-affine deformation. We focus on a simple two-dimensional (2D) model of $Cu_{50}Zr_{50}$ metallic glasses[35] undergoing quasistatic simple shear. We decompose the system into Delaunay triangles, which enables us to calculate exactly the deformation of each triangle at the next strain step in terms of the deformation gradient tensor and the reference triangles at the current strain step. We find several key results. First, using a nudged elastic band method[36–40] to evolve the system from the mechanically stable (MS) state before a stress drop to the resulting MS state after the stress drop, we study the evolution of the non-affine displacement field during stress drops. We find that quadrupolar structures form, move, and dissolve during the stress drops. In addition, we apply small perturbations (dilation, rotation, simple and pure shear) to single triangles in the system, and characterize the resulting non-affine displacement fields following energy minimization in terms of fields set up by point-charges, vortices, dipoles, and quadrupoles. Rotation and simple shear of single triangles give rise to mostly vortices, dilations of single triangles give rise to mostly dipolar fields, and pure shear deformations of single triangles give rise to mostly quadrupolar fields. Since we find that quadrupolar displacement fields predominate during globally applied quasistatic simple shear, these results show that local pure shear deformations of single triangles are the main defects that are excited during bulk, quasistatic simple shear deformations.

The remainder of the article is organized as follows. In Sec. 2, we describe the Lennard-Jones model, the thermal quenching protocol used to generate the zero-temperature glasses, and the athermal, quasistatic simulations of simple shear. In Sec. 3, we present our main results including the accuracy of predictions of the displacement field using the non-affine velocity, the evolution of the non-affine displacement field during stress drops, and the response of the system to local perturbations of single triangles. We provide the conclusions and promising future research directions in Sec. 4. We also include three appendices. In Appendix I, we describe deformations of the local triangles in terms of a rotation matrix, the strain tensor, and its invariants. We then relate these quantities to D_{min}^2, which is frequently used to characterize non-affine displacements[10], in Appendix II. In Appendix III, we describe four order metrics to characterize the resulting displacement fields after applied deformations.

2 Methods

We focus on a simple 2D binary Lennard-Jones model for $Cu_{50}Zr_{50}$ metallic glasses. Atom types A (Zr) and B (Cu) interact via the truncated and force-shifted, pairwise Lennard-Jones (LJ) potential:

$$U_{\alpha\beta}(r_{ij}) = \begin{cases} \phi_{\alpha\beta}(r_{ij}) - \phi_{\alpha\beta}(r_c) - (r_{ij} - r_c)\frac{d\phi_{\alpha\beta}}{dr_{ij}}\Big|_{r_{ij}=r_c}, & r_{ij} < r_c, \\ 0, & r_{ij} \geq r_c \end{cases},$$
(1)

where r_{ij} is the center-to-center separation between atoms i and j, the cutoff distance $r_c = 2.5\sigma_{\alpha\beta}$, α, $\beta = $ A, B, and

$$\phi_{\alpha\beta}(r_{ij}) = 4\epsilon_{\alpha\beta}\left[\left(\frac{\sigma_{\alpha\beta}}{r_{ij}}\right)^{12} - \left(\frac{\sigma_{\alpha\beta}}{r_{ij}}\right)^{6}\right].$$
(2)

The parameters $\sigma_{AA} = 1.0$, $\sigma_{BB} = 0.7975$, $\sigma_{AB} = (\sigma_A + \sigma_B)/2$, $\epsilon_{AA} = 1.0$, and $\epsilon_{BB} = 0.5584$ were chosen to match the sizes and cohesive energies of Zr and Cu.[41] We set $\epsilon_{AB} = (\epsilon_{AA} + \epsilon_{BB})/2 - \Delta H_{mix}$ using the heat of mixing ΔH_{mix} from experiments.[42] The mass ratio for CuZr alloys is $m_A/m_B = 1.435$. In the following, we display the data using LJ units, where lengths, times, stresses, and temperatures are given in units of σ_{AA}, $\sigma_{AA}\sqrt{m_A/\epsilon_{AA}}$, $\epsilon_{AA}/\sigma_{AA}^2$, and ϵ_{AA}/k_B, respectively.

Each system consists of $N = 3600$ atoms (half A and half B) in a square cell with area $\mathscr{A}$ and periodic boundary conditions. We have also carried out studies with $N = 8100$ and 14400 to assess system-size effects as shown in the Electronic Supplementary Information (ESI). The systems are first equilibrated at high temperature $T = 5.0$ (with pressure $P = 10$) in the liquid state well above the melting temperature and then cooled (at fixed pressure) to low temperature $T = 0.005$ using a fast cooling rate of 0.08 to form disordered, glassy states. The first peak in the radial distribution function satisfied $g(r_1) < 6$ for all low-temperature glasses studied. The Nosé-Hoover thermostat and barostat were used to control the temperature and pressure. The low-temperature glasses were then decompressed to reach zero pressure and minimization of the total potential energy $U = \sum_{i>j} U(r_{ij})$, using the conjugate gradient method, was applied to reach zero temperature. We then subject each glassy sample to athermal, quasistatic simple shear (AQS) deformations[20]. Specifically, we apply an affine simple shear strain $\delta\gamma = 2 \times 10^{-6}$ to the current atomic positions, x_i and y_i, such that the new positions satisfy $x_i' = x_i + \delta\gamma y_i$ and $y_i' = y_i$ in concert with Lees-Edwards boundary conditions[43]. After each applied simple shear strain, we perform energy minimization and repeat the process for a total strain of $\gamma = 0.3$. All of the simulations were conducted using the LAMMPS molecular dynamics simulator.[44]

We calculate the stress tensor $\Sigma_{\mu\nu}$ of the system, where μ, $\nu = x$,

y, using the virial expression:[43]

$$\Sigma_{\mu\nu} = \frac{1}{\mathscr{A}} \sum_{i>j=1}^{N} r_{ij\mu} f_{ij\nu}, \tag{3}$$

where $r_{ij\mu}$ is the μth component of the separation vector $\vec{r}_{ij}$ pointing from atom i to atom j and $f_{ij\nu}$ is the νth component of the interparticle force $\vec{f}_{ij}$ on atom i from atom j. The other important quantities, i.e., the strain tensor to characterize the deformations of the Delaunay triangles and order metrics to describe the structure of the atomic displacement fields, are defined in Appendices I and III, respectively.

3 Results

In this section, we describe the results from the simulations of 2D binary Lennard-Jones glasses undergoing athermal, quasistatic simple shear. We first show the shear stress versus simple shear strain for single zero-temperature samples. The shear stress first increases linearly with strain, until a plastic, atomic rearrangement occurs, causing a discontinuous drop in the shear stress. After the stress drop, there is a quasi-linear increase in the shear stress followed by another stress drop. The quasi-linear increases in shear stress, punctuated by discontinuous drops, continue over the full range of strain. We show that the non-affine atomic motion during the quasi-linear segments can be accurately predicted using linear response, while the error in predicting the non-affine motion during the stress drops increases with their magnitude. To better understand the collective motion during stress drops, we implement a nudged elastic band method to identify intermediate states as the system traverses the minimum energy path from an unstable state to a new potential energy minimum. We characterize the deformation of the system using the strain of individual Delaunay triangles. We compare the Delaunay triangle representation of local strain to $D^2_{\min}$, which has been used frequently to characterize non-affine particle motion during AQS. Lastly, we investigate the displacement fields that arise in response to all possible local perturbations of Delaunay triangles and compare them to the displacement fields that occur during bulk AQS.

3.1 Shear stress versus shear strain

In Fig. 1 (a), we plot the shear stress Σ_{xy} as a function of the imposed simple shear strain γ for a single sample during continuous AQS in the forward direction. As found in previous studies, Σ_{xy} versus γ possesses quasi-linear elastic segments that are punctuated by discontinuous drops in the shear stress.[16,19,20,45,46] Serrated stress-strain curves have been observed in experiments of compressed metallic glasses at low strain rates.[47–49] To unambiguously identify all of the shear stress drops, we also perform a series of one-step backward AQS steps, with the same $\delta\gamma$ as that of AQS in the forward direction, at each γ. This method yields a pair of mechanically stable configurations at the same applied strain γ, one from forward AQS and one from one-step backward AQS, as shown in Fig. 1 (b). At most strains, the shear stress from forward AQS, $\Sigma_{xy}(\gamma)$, is the same as that for one-step backward AQS, $\Sigma'_{xy}(\gamma)$. The shear stress of the two configurations is different at the discontinuous stress drops. In the inset to Fig. 1 (b), we plot
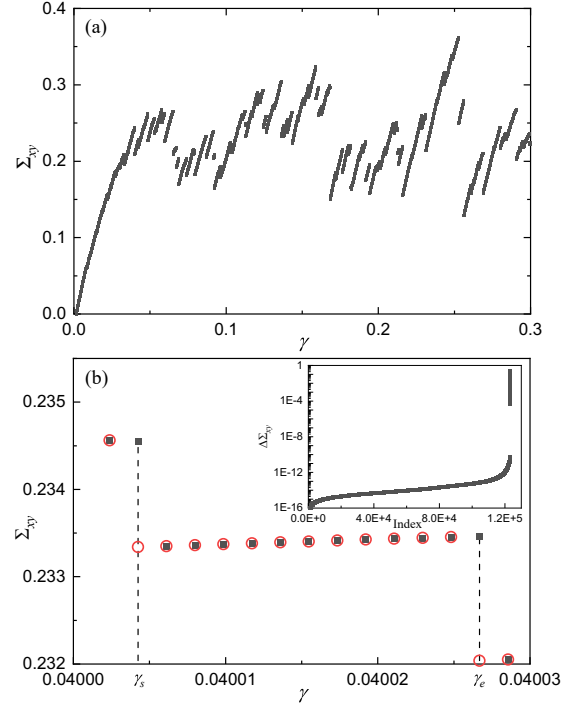

Fig. 1 (a) Shear stress Σ_{xy} versus simple shear strain γ for a single zero-temperature configuration during athermal, quasistatic shear (AQS). (b) Close-up of the data in (a). The black-filled squares indicate AQS in the forward direction, and the red open circles indicate one-step backward AQS from the configuration with a strain value immediately above it. The shear strains γ_s and γ_e give the start and end of a quasi-elastic segment with no discontinuous stress drops. Inset: The shear stress difference $\Delta\Sigma_{xy} = |\Sigma_{xy}(\gamma) - \Sigma'_{xy}(\gamma)|$ between a configuration obtained through AQS in the forward direction, Σ_{xy}, and that obtained through AQS in the backward direction from the strain value immediately above it, Σ'_{xy}, sorted in ascending order.

the magnitudes of the shear stress differences $\Delta\Sigma_{xy} = |\Sigma_{xy} - \Sigma'_{xy}|$ in ascending order for the AQS trajectory in Fig. 1 (a). For the continuous, quasi-elastic segments, the magnitudes of the shear stress differences satisfy $10^{-16} < \Delta\Sigma_{xy} < 5 \times 10^{-11}$. There is a gap of roughly six orders of magnitude between the small shear stress differences caused by errors in force balance (in the continuous quasi-elastic segments) and the true stress drops that satisfy $5 \times 10^{-5} < \Delta\Sigma_{xy} < 0.23$. Immediately after a stress drop, a quasi-elastic segment begins at γ_s and ends at the next stress drop at γ_e.

Within linear response, the non-affine atomic motion during AQS can be predicted using

$$H_{ij} \frac{d\vec{r}_j}{d\gamma} = -\vec{\Xi}_i, \tag{4}$$

where $\vec{r}_j = (x_j, y_j)$ gives the coordinates of the jth atom, $H_{ij} = \frac{\partial^2 U}{\partial r_i \partial r_j}$ is the Hessian matrix, and $\vec{\Xi}_i = \frac{\partial^2 U}{\partial \vec{r}_i \partial \gamma}$ is the force on atom i that is induced when the system is subjected to an affine simple shear deformation.[20] Using Eq. 4, the predicted atomic positions

(x_i^p, y_i^p) at the next strain $\gamma + \delta\gamma$ are

$$x_i^p = x_i + \delta\gamma y_i + \delta\gamma \frac{dx_i}{d\gamma}, \quad (5)$$

$$y_i^p = y_i + \delta\gamma \frac{dy_i}{d\gamma}. \quad (6)$$

After applying Eqs. 5 and 6 iteratively, we can estimate the target atomic positions at the end of each quasi-elastic segment (at γ_e) using the reference atomic positions from the start of each segment (at γ_s). In addition, we can predict the target atomic positions after each shear stress drop using the reference atomic positions before the shear stress drop.

We can obtain the error in the predicted atomic positions by calculating the magnitude-squared of the difference $(\Delta R)^2 = |\vec{R}^p - \vec{R}^s|^2/N$ between the predicted atomic configurations $\vec{R}^p$ and those directly from the AQS simulations, $\vec{R}^s$, where $\vec{R} = (x_1, y_1, \ldots, x_N, y_N)$. In Fig. 2, we show a scatter plot of $(\Delta R)^2$ versus the magnitude of the difference in shear stress $\Delta\Sigma_{xy}$ between the target and reference configurations for quasi-elastic segments and shear stress drops. For most systems, we obtain extremely accurate predictions for the atomic positions at the ends of the quasi-elastic segments, $(\Delta R)^2 \sim 10^{-8}$ using $\delta\gamma = 2 \times 10^{-6}$. (For a few quasi-elastic segments, the predictions generated Hessians with negative eigenvalues, which give larger values of $(\Delta R)^2$.) In contrast, $(\Delta R)^2 \sim \Delta\Sigma_{xy}^2$ scales quadratically with the magnitude of the shear stress difference for the shear stress drops, and $(\Delta R)^2$ does not decrease with decreasing $\delta\gamma$. Thus, predictions of the atomic positions after stress drops are only accurate for extremely small stress drops using this method. In the next section, we will introduce an approach for predicting the non-affine aotmic motion during large stress drops.
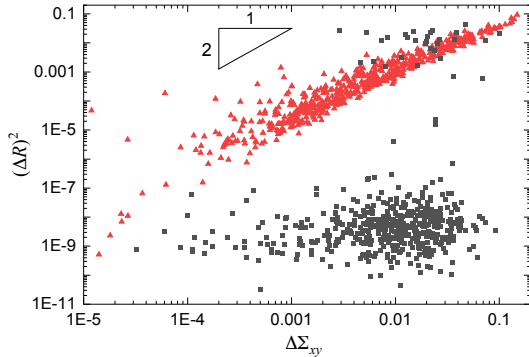

Fig. 2 The magnitude-squared of the difference between the predicted target and reference configurations $(\Delta R)^2 = |\vec{R}^p - \vec{R}^s|^2/N$ as a function of the magnitude of the shear stress difference $\Delta\Sigma_{xy}$ between the target and reference configurations. Data for the quasi-elastic segments (shear stress drops) are shown as black squares (red triangles). The start of each quasi-elastic segment is used as the reference to predict the target configuration at the end of the quasi-elastic segment. The reference and target configurations for the shear stress drops correspond to those immediately before and after the stress drop.

In Fig. 3 (a) and (b), we display the non-affine displacement fields near the beginning and near the end of a particular quasi-elastic segment. In both displacement fields, we find Eshelby-

like quadrupolar structures.[1,20,26,50] During this quasi-elastic segment, the quadrupolar structure on the right side of the image in (a) dissolves with increasing strain and a new one on the left side of the image forms in (b). Movies of the evolution of the non-affine displacement fields during quasi-elastic segments are shown in the ESI. We find that even though complex collective atomic motion occurs frequently during the quasi-elastic segments, the displacement fields at the ends of the quasi-elastic segments can be predicted accurately using the configurations at the start of the quasi-elastic segments and Eqs. 5 and 6.

In Fig. 3 (c), we show the non-affine displacement field calculated using the last configuration of a quasi-elastic segment and a configuration immediately after the shear stress drop that ended the previous quasi-elastic segment. We identify two distinctive quadrupolar structures in the displacement field. However, if we employ Eqs. 5 and 6 to predict the non-affine displacement field using the last configuration of the previous quasi-elastic segment, we obtain the displacement field in Fig. 3 (d), which only includes a single quadrupolar structure. The non-affine displacement fields in Fig. 3 (c) and (d) are clearly different. These results emphasize again that the approach of using the atomic configuration immediately before a shear stress drop plus linear response is not sufficient to accurately predict the atomic configuration after shear stress drops.
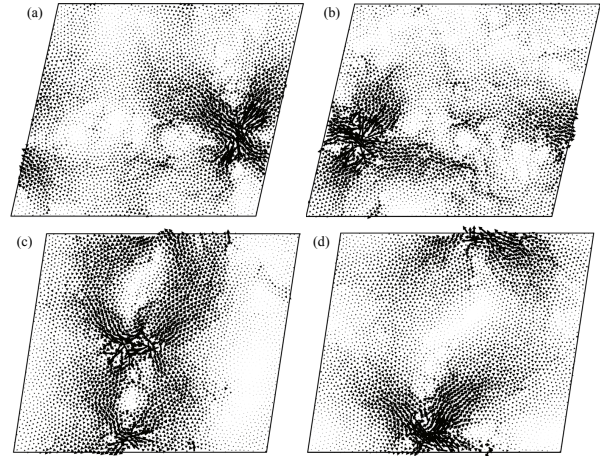

Fig. 3 Non-affine displacement fields normalized to unity for quasi-elastic segments and shear stress drops. The non-affine displacement fields in (a)-(c) were obtained by comparing atomic configurations separated by $\delta\gamma$ in a quasi-elastic segment. The displacement fields in (a) and (b) correspond to configurations at 0.32 and 0.999 of the length of a particular quasi-elastic segment, respectively. The displacement field in (c) corresponds to a shear stress drop, and the configurations before and after the shear stress drop were used to calculate the displacement field. (d) The non-affine displacement field predicted using Eqs. 5 and 6 and the atomic configuration before the shear stress drop in (c).

3.2 Minimum energy paths during shear stress drops

As shown in the previous section, if the shear stress drop is large, one cannot predict the atomic configuration after the stress drop using linear response applied to the atomic configuration immediately before the stress drop. In this section, we describe a nudged
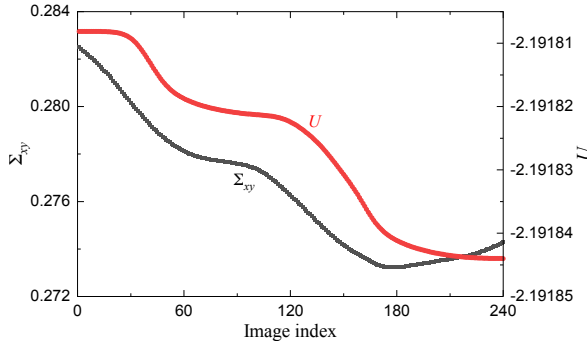
Fig. 4 The shear stress Σ_{xy} (solid black line) and the total potential energy U (solid red line) as a function of the index of roughly equally spaced images in ΔR along the minimal energy path from the configuration immediately before to that after the shear stress drop in Fig. 3 (c).

elastic band (NEB) method to obtain the atomic configurations that occur along a minimal energy path between the configuration before the shear stress drop and the new mechanically stable configuration after the drop.[36–40] A series of configurations (called images) is generated by linearly interpolating in configuration space between the initial and final mechanically stable states. To do this, springs are added between successive images to ensure equal spacing ΔR between the images. The total force acting on each atom in image i is the sum of two contributions,

$$\vec{F}_i = \vec{F}_i^{\perp} + \vec{F}_i^{\parallel}, \tag{7}$$

where $\vec{F}_i^{\perp}$ is the force arising from the interatomic potential energy,

$$\vec{F}_i^{\perp} = \vec{\nabla} U(\vec{R}_i) \cdot \hat{\tau}_i \hat{\tau}_i - \vec{\nabla} U(\vec{R}_i), \tag{8}$$

and $\vec{F}_i^{\parallel}$ is the spring force between successive images,

$$\vec{F}_i^{\parallel} = k(|\vec{R}_{i+1} - \vec{R}_i| - |\vec{R}_i - \vec{R}_{i-1}|)\hat{\tau}_i, \tag{9}$$

where $\hat{\tau}_i = \vec{\tau}_i / |\vec{\tau}_i|$ is the normalized local tangent of image i,

$$\vec{\tau}_i = \frac{\vec{R}_i - \vec{R}_{i-1}}{|\vec{R}_i - \vec{R}_{i-1}|} + \frac{\vec{R}_{i+1} - \vec{R}_i}{|\vec{R}_{i+1} - \vec{R}_i|}, \tag{10}$$

$k = 1$ is the spring constant that ensures the images are equidistant in configuration space, and $\vec{R}_i$ is the atomic configuration for image i. An optimization algorithm using a Verlet integration scheme is used to move the image configurations such that $\vec{F}_i = 0$ for all i.[36]

In Fig. 4, we plot the shear stress Σ_{xy} and total potential energy U as a function of the image index along a minimal energy path for the shear stress drop in Fig. 3 (c). Σ_{xy} and U evolve continuously from the values immediately before the shear stress drop to those after. ΔR and $\Delta \Sigma_{xy}$ between successive images are controlled by the total number of images, n. We chose n such that $\Delta R \sim 10^{-8}$ and $\Delta \Sigma_{xy} \sim 10^{-5}$ between successive images. In contrast, the average shear stress drop $\langle \Delta \Sigma_{xy} \rangle \approx 10^{-2}$ for forward AQS. Using this method, we will calculate the non-affine displacement field and the local strain tensor by comparing successive images in the next

section.

3.3 Evolution of the displacement field

To characterize the local strain field during AQS, we perform Delaunay triangulation using the atom centers as the vertices at each strain γ. Local strains at the atomic scale are then characterized through deformations of the triangles. Note that triangles in two spatial dimensions (2D), or tetrahedra in 3D, represent the largest grouping of atoms for which the deformation of the system can be measured without any loss of information about the atomic motion. Specific details concerning the definition of the strain tensor from the Delaunay triangulation are provided in Appendix I.

In Fig. 5 (a), we show the von Mises strain $\varepsilon_{\alpha}^{vm}$ of each triangle α by comparing the two triangulations before and after the shear stress drop in Fig. 3 (c). The triangles with relatively high von Mises strain coincide with the locations of the quadrupolar structures in Fig 3 (c). However, as discussed in the previous section, to develop the ability to predict the atomic configurations after shear stress drops, we must understand the evolution of the atomic configurations along minimal energy paths during the shear stress drops. Thus, we also calculate the von Mises strain of each triangle as the system moves along a minimal energy path from the beginning to the end of shear stress drops. In Fig. 5 (b)-(d), we show the von Mises strain for each triangle near the beginning, middle, and end of the minimal energy path associated with the shear stress drop in Fig. 3 (c). The regions of large von Mises strain in panel (a) and those in panels (b)-(d) do not coincide. Moreover, the large strain regions in (b)-(d) dissolve and other large-strain regions form along the minimal energy path.

To further illustrate the evolution of the large-strain regions as a function of image index along a minimal energy path during shear stress drops, we break up the atomic configurations into subsystems. We consider triangles within rectangular sections (as shown in Fig. 5 (a)) with height $7\sigma_{AA}$ and equal-sized bins in the horizontal direction with width σ_{AA}. The average von Mises strain for the ith bin in a given rectangular section is

$$\langle \varepsilon^{vm} \rangle_i = \sum_{\alpha=1}^{n_i} \frac{A_{i\alpha}}{A_i} \varepsilon_{\alpha}^{vm}, \tag{11}$$

where n_i is the total number of triangles within the ith bin, $A_{i\alpha}$ is the area of triangle α that is included in the ith bin, A_i is the area of the ith bin, and $\varepsilon_{\alpha}^{vm}$ is the von Mises strain of triangle α. In Fig. 6, we show the average von Mises strain for each bin (along the vertical axis) in the rectangular subsystems in Fig. 5 (a) as a function of the image index along the minimal energy path (along the horizontal axis). Note that the sizes of the rectangular regions are scaled so that the images appear in a square format.

We make several observations about the evolution of the strain field during the shear stress drop depicted in Fig. 5 (a). First, regions of large-strain form and dissolve during the shear stress drop. In Fig. 6 (a), a large-strain region forms near the initial image and ends near image 70. Another large-strain region begins to form near image 220. In Fig. 6 (b), two nearby large-strain regions form near image 100; the top one dissolves around image
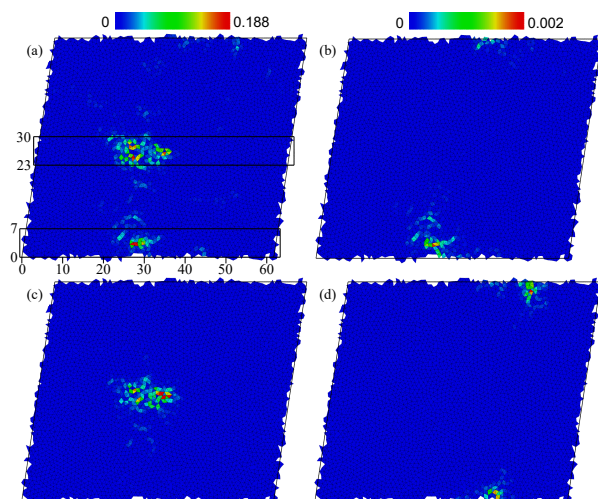
Fig. 5 The von Mises strain ε_α^{vm} of each triangle α during the shear stress drop in Fig. 3 (c). (a) The von Mises strain calculated by comparing the Delaunay triangulations immediately before and after the shear stress drop. Evolution of the strain for the triangles within the two rectangular boxes along the minimal energy path is shown in Fig. 6. (b)-(d) The von Mises strain at image indexes $\lambda = 10$, 110, and 230 at early, intermediate, and end stages of the minimal energy path during the shear stress drop. The reference triangulations are from images $\lambda - 1$. The color scales from blue to red indicate increasing von Mises strain (over the range $[0, 0.188]$ for (a) and $[0, 0.002]$ for (b)-(d)).

Fig. 6 The average von Mises strain $\langle \varepsilon^{vm} \rangle_i$ in each bin i (vertical axis) for the (a) bottom and (b) top rectangular regions in Fig. 5 (a) as a function of the image index (horizontal axis) along the minimal energy path during the shear stress drop in Fig. 5 (a). The color scale for $\langle \varepsilon^{vm} \rangle_i$ increases from blue to red over the range $[0, 0.001]$. The solid white lines highlight the spatio-temporal evolution of two of the large-strain regions.
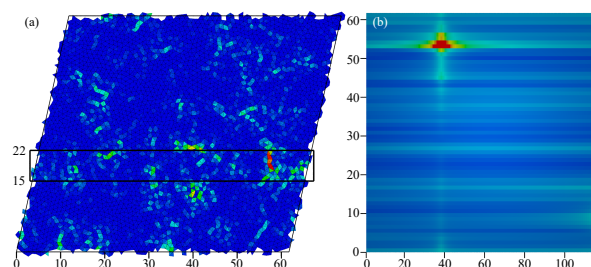
Fig. 7 (a) The von Mises strain ε_α^{vm} for each triangle for the quasi-elastic segment in Fig. 3 (a) and (b). The strain is obtained by comparing the triangulations from the start and end of the quasi-elastic segment. (b) Evolution of the average von Mises strain $\langle \varepsilon^{vm} \rangle_i$ (bin index versus image index) for triangles within the rectangular boxed region in (a) during the same quasi-elastic segment in (a), which includes the two quadrupolar structures of the non-affine displacement field in Fig. 3 (a) and (b). The strain is obtained by comparing the triangulations from configurations separated by $\delta\gamma$. The range of the color scales is $[0, 0.1]$ for (a) and $[0, 0.001]$ for (b).

140, and the other dissolves around image 180. Second, the large-strain regions do not form and dissolve abruptly. For example, one side of the large-strain region in Fig. 6 (a) dissolves before the other. Similarly, one side of one of the large-strain regions forms before the other in Fig. 6 (b). These results imply the existence of a wave speed for the evolution of large-strain regions during shear stress drops. A more complete visualization of the spatio-temporal evolution of the large-strain regions during this shear stress drop is included as a movie in the ESI.

Previous studies of AQS applied amorphous solids have shown that although the particle dynamics is reversible, significant non-affine motion frequently occurs during the quasi-elastic segments.[51,52] We find that quadrupolar structures in the non-affine displacement fields also appear during quasi-elastic segments (as shown in Fig. 3 (a) and (b)). Thus, we find similar results for the spatio-temporal evolution of large non-affine strain regions during quasi-elastic segments and during stress drop. In Fig. 7 (a), we show the von Mises strain for each triangle by comparing the triangulations at the beginning and end of the quasi-elastic segment depicted in Figs. 3 (a) and (b). When the configurations at the beginning and end of the quasi-elastic segment are compared, the large-strain regions are randomly distributed throughout the system. In contrast, if we compare configurations separated by small simple shear strain increments $\delta\gamma$, we can track the spatio-temporal evolution of the large-strain regions. For example, if we focus on the regions of the system that feature the two quadrupolar structures in Figs. 3 (a) and (b) (i.e., the rectangular boxed region in Fig. 7 (a)), we find that a region of large strain forms near image 30 and ends near 50 and another large-strain region
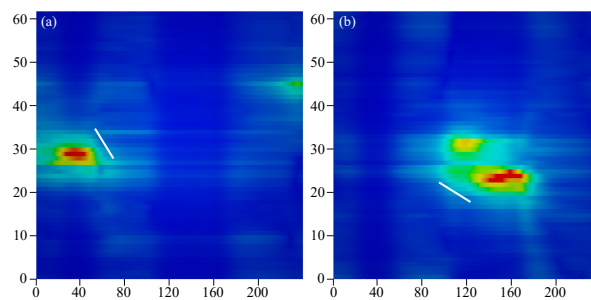
begins to form near image 120. Note that the rest of the system is quiescent with extremely small strain. Movies of the spatio-temporal evolution of the large-strain regions during quasi-elastic segments are included in the ESI.

3.4 Advantage of triangle representation of displacement field

Numerous prior studies have employed $D_{\min}^2$ to characterize the non-affine displacement fields of amorphous materials during applied strain;[4,10,18,32,53,55] $D_{\min}^2$ measures the deviation of the displacement of each atom and its neighbors from a local affine deformation.[10] (See Appendix II for the definition of $D_{\min}^2$ and the deformation gradient tensor G_i associated with each atom i.) In this section, we compare measurements of non-affine atomic motion using the deformation gradient tensor F_α associated with each Delaunay triangle α and the deformation gradient tensor G_i, associated with each atom i, obtained by calculating $D_{\min}^2$ (i.e., minimizing the local non-affine motion).

The deformation gradient tensor F_α is defined for each triangle α, however, G_i is defined for each atom i. To make the compari-

son between the two quantities, we calculate the average triangle deformation gradient tensor associated with each atom i:

$$\overline{F}_i = \sum_{\alpha=1}^{n_i} \frac{A_{i\alpha}}{A_i} F_\alpha, \qquad (12)$$

where n_i is the number of Delaunay triangles connected to atom i, $A_{i\alpha}$ is the area of each triangle α associated with atom i, and $A_i = \sum_\alpha A_{i\alpha}$. In Fig. 8, we show that each of the four components (xx, xy, yx, and yy) of the average triangle deformation gradient tensor $\overline{F}_i$ is linearly related to the corresponding component of G_i (with a coefficient close to 1). Thus, the deformation gradient tensor G_i associated with D_{min}^2 is an average of the triangle deformation gradient tensor over all triangles that include atom i as a vertex.

An advantage of using F_α is that it is the most local deformation gradient tensor that can be defined for an atomic system. To illustrate this feature, consider the atoms numbered 1, 2, 3, and 4 in Fig. 9 (a) and (b) and the local rotation ω, which is an invariant of the deformation gradient tensor as discussed in Appendix I. These atoms belong to triangles with both positive and negative rotation angles (using the triangle deformation gradient tensor in Fig. 9 (b)), which results in a near-zero value for the rotation when D_{min}^2 is calculated for each atom. (See Fig. 9 (a).) Similarly, atoms 1, 2, 5, and 6 possess near-zero hydrostatic strain (Fig. 9 (c)) when using D_{min}^2 to define G_i, since these atoms belong to triangles with both positive and negative volume changes, ε^{hyd} (Fig. 9 (d)). Thus, all information concerning local atomic deformation is stored in the deformation gradient tensor F_α for each Delaunay triangle α; calculating D_{min}^2 results in a loss of information.

Fig. 9 (a)-(d) Comparison of the invariants (rotation angle ω, top row, and ε^{hyd}, bottom row) of the deformation gradient tensors G_i (left column) associated with each atom i and F_α associated with each triangle α. The color scale for values of ω and ε^{hyd} increases linearly from blue to red.

3.5 Response to local perturbations

As shown in previous sections, quadrupolar displacement fields occur during both the quasi-elastic segments and the abrupt shear stress drops in systems undergoing athermal, quasistatic simple shear. Do other types of displacement fields occur during AQS? In this section, we apply four types of perturbations (rotation, dilation, simple and pure shear) to individual triangles in the system and characterize the structure of the resulting displacement fields. (See Fig. 10 (a).) After performing a given perturbation, we fix the displaced atoms in the selected triangle and perform potential energy minimization for the rest of the system. To ensure linear response, we set small magnitudes for the perturbations: the rotation angle $\theta \sim 10^{-8}$ rad and the atomic displacements for the other perturbations $d \sim 10^{-8}$. We characterize the response of the system by comparing the resulting displacement fields to idealized vortex, dipolar, and quadrupolar displacement fields, as shown in Fig. 10 (b)-(d).

We consider four order metrics, each defined within the range 0 to 1, to characterize the displacement field in response to the local perturbations. The "circulation" Γ measures the degree to which the displacement field rotates around a point, the "flux" Φ describes the magnitude of the flow outward/inward of the displacement field, and the bond-orientational order parameters, ψ_2, and ψ_4,[56] quantify the extent to which the displacement fields are oriented in a single direction or in two perpendicular directions. Mathematical expressions that define the four order metrics are provided in Appendix III. Displacement fields with large values of Γ and small values of Φ, ψ_2, and ψ_4 are identified as vortex-like structures, displacement fields with small values of Γ and large values of Φ, ψ_2 and ψ_4 correspond to dipolar structures, and displacement fields with small values of Γ, Φ, and ψ_2, but large values for ψ_4 correspond to quadrupolar structures.

As shown in Fig. 11, the local perturbations applied to the zero-strain glasses give rise to a wide range of defects in the displacement field. Rotation (Column (a)) and simple shear (Column (b))
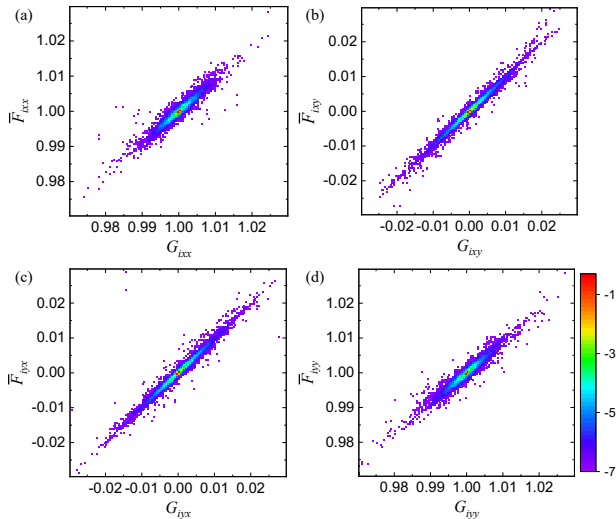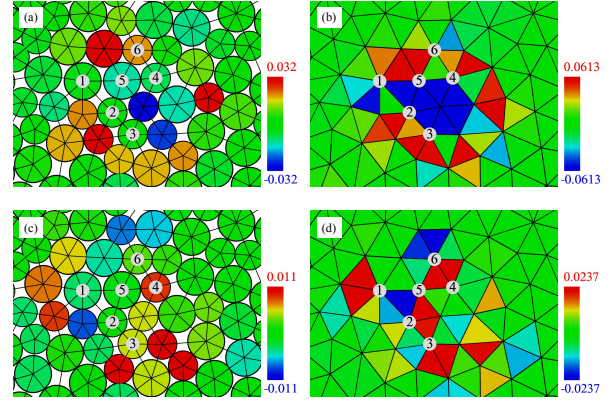

Fig. 8 Probability distributions of the components of the average triangle deformation gradient tensor $\overline{F}_i$ and the deformation gradient tensor G_i associated with D_{min}^2 for atom i using the same data in Fig. 12. (a) $P(\overline{F}_{ixx}, G_{ixx})$, (b) $P(\overline{F}_{ixy}, G_{ixy})$, (c) $P(\overline{F}_{iyx}, G_{iyx})$, and (d) $P(\overline{F}_{iyy}, G_{iyy})$. The probability increases from blue to red on a $\log_{10}$ scale.

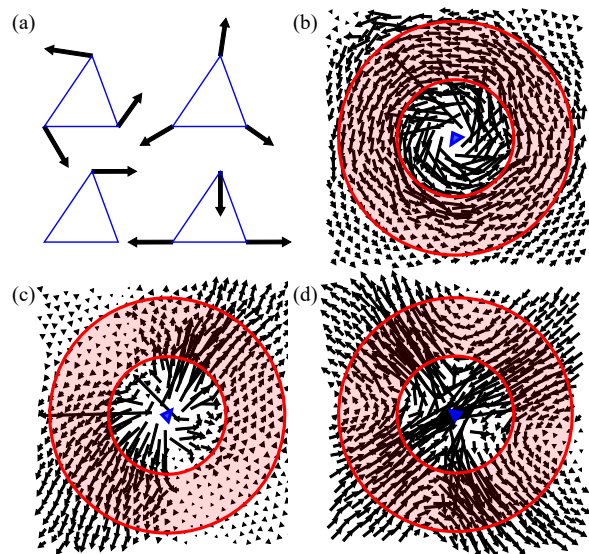**Soft Matter Accepted Manuscript**

Fig. 10 (a) Four types of perturbations applied to single triangles: rotation (upper left), dilation (upper right), simple shear (lower left), and pure shear (lower right). The response of the perturbations can be compared to idealized (b) vortex, (c) dipolar, and (d) quadrupolar displacement fields. The order metrics described in Appendix III are calculated in the annular region between the two red circles.

applied to single triangles give rise to vortex-like structures (with moderate values of Γ). In contrast, dilations (Column (c)) applied to single triangles induce dipole-like structures with elevated values of Φ, ψ_2, and ψ_4. Pure shear of single triangles gives rise to quadrupolar structures with large values of ψ_4.

Which of the local perturbations does bulk, quasistatic simple shear flow activate? To address this question, we focus on the images along minimal energy paths during shear stress drops. For each image during the minimal energy path, we identify the disk region (with radius $5.5\sigma_{AA}$) surrounding a given triangle with the largest average von Mises strain. We then calculate the four order metrics for the non-affine displacement field between successive images in an annular region surrounding this triangle (with inner radius $5.5\sigma_{AA}$ and outer radius $11\sigma_{AA}$). In Fig. 12, we show the probability distributions, $P(\Phi, \Gamma)$, $P(\psi_2, \Gamma)$, and $P(\psi_4, \Gamma)$, for 232 shear stress drops. The defects that occur during bulk, quasistatic simple shear are similar to those generated by *local pure shear* in Fig. 11 (d). Thus, local pure shear deformations of single triangles are the main defects that are activated during bulk, quasistatic simple shear, giving rise to mainly quadrupolar non-affine displacement fields.

4   Conclusions and future directions

In this article, we studied the non-affine atomic motion that occurs in a 2D Lennard-Jones model of metallic glasses subjected to athermal, quasistatic simple shear (AQS). The shear stress versus strain curve consists of continuous, quasi-elastic segments punctuated by abrupt shear stress drops, which correspond to atomic rearrangements. Using a novel method to define the deformation gradient tensor associated with triangular elements from Delau-

nay triangularization and by following minimal energy paths during shear stress drops, we obtained several key results concerning the mechanical response of amorphous materials. First, we showed that collective structures in the non-affine displacement fields that occur during the quasi-elastic segments are similar to those that occur during stress drops. Quadrupolar displacement fields, which are the most common collective structures, form and dissolve both during the quasi-elastic segments and during shear stress drops. Second, we emphasized that the common procedure of using only the mechanically stable configurations immediately before and after a stress drop to define the non-affine displacement field is problematic since the system can move significantly in configuration space during the stress drop. By following minimal energy paths during the shear stress drops, we tracked the spatio-temporal evolution of multiple quadrupolar structures in the system using successive configurations that differ by a small amount in stress. Third, we compared the deformation gradient tensor F_α associated with each triangle α to the atomic deformation gradient tensor G_i defined by $D^2_{\min}$, and show that G_i is an average of F_α over adjacent triangles. Thus, an advantage of using F_α with triangular elements is that it is the largest grouping of atoms in 2D that captures all information concerning the atomic motion. Lastly, by studying the response of the system to perturbations of single triangles, such as rotation, dilation, simple and pure shear, we demonstrated that vortex-like, dipolar, and quadrupolar displacement fields can be triggered. Local rotation and simple shear perturbations generate vortex-like displacement fields; local dilation generates dipolar displacement fields; and local pure shear generates quadropolar displacement fields. Since bulk AQS typically gives rise to quadrupolar displacement fields, these results emphasize that bulk AQS activates mainly local pure shear strains of triangles.

These results raise several important, open questions for future research. First, we showed that bulk, quasistatic simple shear gives rise to local pure shear strains of triangles, which generate quadrupolar displacement fields. Can vortex-like or dipolar displacement fields be generated by other bulk deformations, such as uniaxial tension, and spatially non-uniform deformations, such as indentation? A microscopic theory for the non-affine displacement fields in amorphous should be able to calculate the fraction of each type of triangle strain that is activated for a given macroscopic deformation. If so, the theory will be able to predict the resulting non-affine displacement field for a given applied macroscopic deformation. In addition, the methodology introduced in this article can be generalized to 3D using Delaunay tetrahedralization to uniquely define the deformation gradient tensor for each tetrahedron with atoms at its vertices. Other studies will include monitoring the evolution of the displacement fields during applied strain at finite strain rates and non-zero temperature, which are essential for making comparisons to experimental studies of glasses.

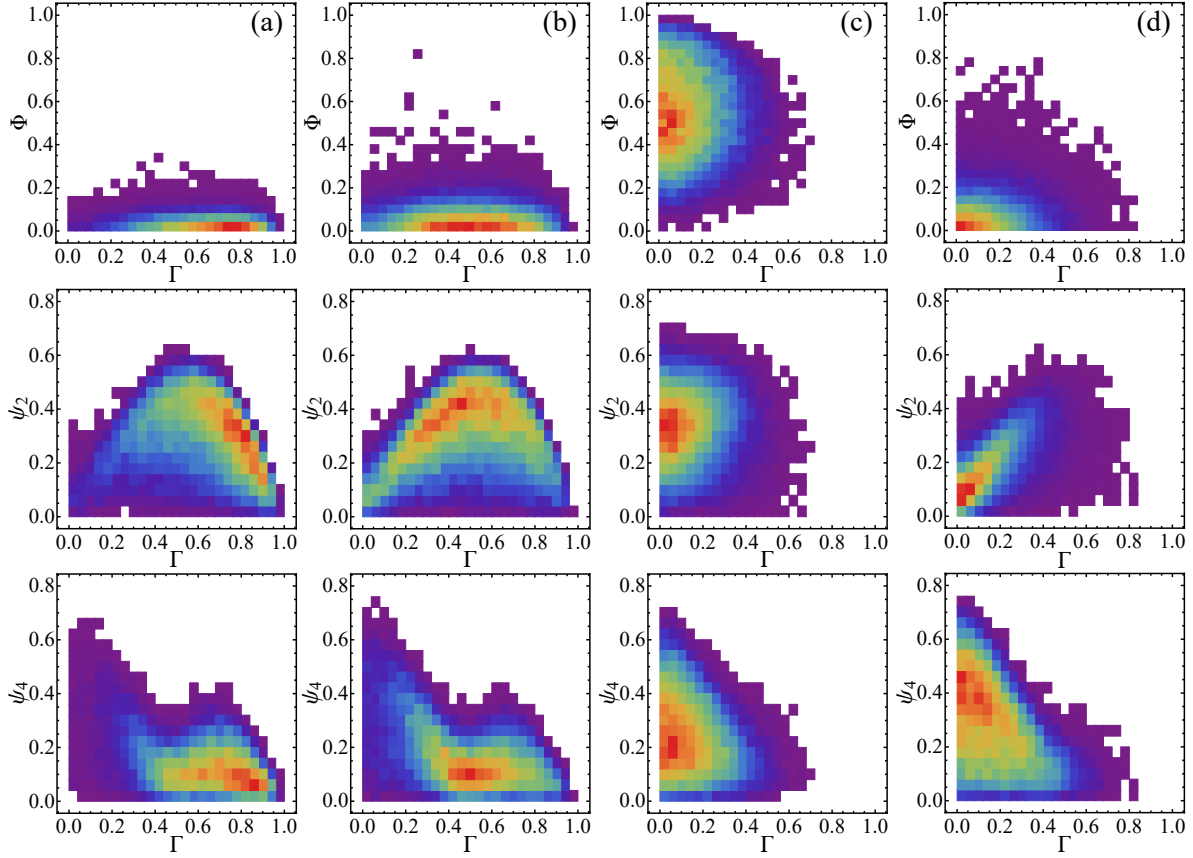## Conflicts of interest

There are no conflicts to declare.

Fig. 11 Probability distributions of different combinations of the order metrics, $P(\Phi,\Gamma)$ (top row), $P(\psi_2,\Gamma)$ (middle row), and $P(\psi_4,\Gamma)$ (bottom row), for the non-affine displacement fields in response to four different perturbations: Column (a) rotation, Column (b) simple shear, Column (c) dilation, and Column (d) pure shear. The data is obtained from uniformly sampling 570 unstrained glasses. The color scale from blue to red indicates increasing probability on a linear scale.

Appendix I: Deformation of triangular elements

Each Delaunay triangle includes three vertex atoms with a total of six degrees of freedom. Motion of each triangle can be decomposed into three parts: translation of its geometric center, rotation about its geometric center, and changes in the shape of the triangle. Let $\vec{r}_i^0$ and $\vec{r}_i^n$ ($i = 1, 2, 3$) be the Cartesian coordinates of the three vertex atoms of the reference and the deformed triangular element α, respectively. The translation vector $\vec{u}_c = \frac{1}{3}\sum_{i=1}^{3}(\vec{r}_i^n - \vec{r}_i^0)$ corresponds to two degrees of freedom. The vector $\vec{r}_{ij}^0 = \vec{r}_i^0 - \vec{r}_j^0$ connects two vertices i and j of the reference triangle, while $\vec{r}_{ij}^n = \vec{r}_i^n - \vec{r}_j^n$ connects the same pair of atoms of the deformed triangle. The deformation gradient tensor F_α transforms the edge vector $\vec{r}_{ij}^0$ into $\vec{r}_{ij}^n$. F_α can be obtained using any two of the three edges of the triangular element α, e.g.,

$$F_\alpha = \begin{bmatrix} x_{i2}^n & x_{i3}^n \\ y_{i2}^n & y_{i3}^n \end{bmatrix} \begin{bmatrix} x_{i2}^0 & x_{i3}^0 \\ y_{i2}^0 & y_{i3}^0 \end{bmatrix}^{-1}, \qquad (13)$$

where triangle α has vertices i, 2, and 3 as shown in Fig. 13. F_α contains the remaining four degrees of freedom. The deformation gradient tensor F_α can be decomposed into a rotation matrix R_α and a symmetric matrix U_α: $F_\alpha = R_\alpha U_\alpha$. The matrix R_α represents a rotation with an angle of ω_α about the z-axis.

The local Green-Lagrangian strain tensor E_α is defined for each triangle α as $E_\alpha = (F_\alpha^{\mathrm{T}} F_\alpha - I)/2 = (U_\alpha^{\mathrm{T}} U_\alpha - I)/2$, where I is the identity matrix. E_α can be decomposed into the sum of hydrostatic and deviatoric strains as follows

$$E_\alpha = \varepsilon_\alpha^{hyd} I + E_\alpha'. \qquad (14)$$

The hydrostatic strain,

$$\varepsilon_\alpha^{hyd} = \frac{\mathrm{tr}E_\alpha}{2} = \frac{(\varepsilon_{11} + \varepsilon_{22})}{2}, \qquad (15)$$

is closely related to the volume change of the triangle, while the deviatoric strain tensor E_α' is related to shear deformations at constant volume. The von Mises strain is defined as

$$\varepsilon_\alpha^{vm} = \sqrt{\frac{1}{2}\mathrm{tr}(E_\alpha'^2)}. \qquad (16)$$
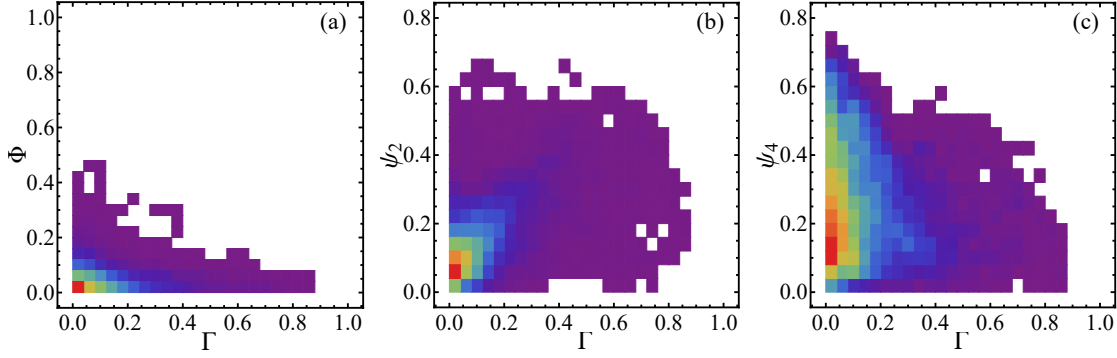
Fig. 12 Probability distribution of different combinations of the order metrics, (a) $P(\Phi, \Gamma)$, (b) $P(\psi_2, \Gamma)$, and (c) $P(\psi_4, \Gamma)$, for the non-affine displacement fields of all images along the minimal energy paths for 232 shear stress drops. The color scale from blue to red indicates increasing probability on a linear scale.

Appendix II: Relation between D^2_{min} and triangle deformation gradient tensor

The D^2_{min} quantity introduced by Falk and Langer[10] provides a measure for the deviations of atomic motion from local affine deformation. Suppose we define the deviation,

$$D_i^2 = \sum_{j=1}^{n_i} |\vec{r}_{ij}^n - G_i \vec{r}_{ij}^0|^2, \tag{17}$$

where n_i is the number of neighboring atoms surrounding a reference atom i (e.g. using a distance cutoff set by the first minimum in the radial distribution function). D_i^2 is minimized by finding the best-fit local deformation gradient tensor,

$$G_i = X_i Y_i^{-1}, \tag{18}$$

where

$$X_i = \sum_{j=1}^{n_i} \vec{r}_{ij}^n (\vec{r}_{ij}^0)^T \tag{19}$$

and

$$Y_i = \sum_{j=1}^{n_i} \vec{r}_{ij}^0 (\vec{r}_{ij}^0)^T. \tag{20}$$

The rotation angle ω_i and other invariants, such as the von Mises ε_i^{vm} and hydrostatic ε_i^{hyd} strains associated with atom i can be obtained from the deformation gradient tensor G_i after minimization.

To define the triangle deformation gradient tensor, we first perform a Delaunay triangularization for the N atoms. The reference atom i and its neighbors j $(j = 1, 2, ..., n_i)$ are shown in Fig. 13. The deformation of the separation vector $\vec{r}_{ij}$ between reference atom i and its neighbors can be expressed as

$$\vec{r}_{ij}^n = F_j \vec{r}_{ij}^0, \tag{21}$$

where F_j is the deformation gradient tensor of the triangle with vertices i, j, and $(j+1)'$ and $(j+1)' = (j+1) \mod n_i$. Thus, we can relate the deformation gradient tensors G_i and F_j by substituting
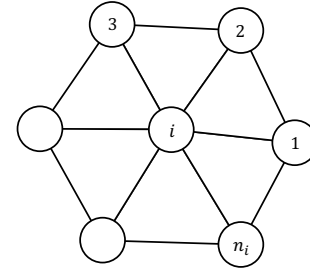

Fig. 13 A reference atom i and its neighboring atoms j $(j = 1, 2, ..., n_i)$ identified by Delaunay triangularization and indexed in counterclockwise order. Adjacent pairs of neighbors together with the reference atom i form the Delaunay triangles associated with atom i.

Eq. 21 into Eq. 18:

$$G_i = \sum_{j=1}^{n_i} F_j W_j, \tag{22}$$

where the weighed matrix

$$W_j = \vec{r}_{ij}^0 (\vec{r}_{ij}^0)^T Y_i^{-1}. \tag{23}$$

Appendix III: Order metrics for non-affine displacement field

In Sec. 3.5, we described the response of the system to local perturbations of individual triangles. In particular, we calculated several order metrics that characterize the displacement field in an annular region surrounding the perturbed triangle as shown in Fig. 10 (b)-(d). We set the inner and outer radii to be $5.5\sigma_{AA}$ and $11\sigma_{AA}$, respectively. Changing the values of the radii does not alter the key features of the order metrics. In this Appendix, we provide the mathematical expressions that define the four order metrics discussed in the main text.

To calculate the average "circulation" of the displacement field within the annular region, we define

$$\Gamma = \frac{1}{C} \left| \sum_{j=1}^{n_a} \hat{r}_{cjx} v_{jy} - \hat{r}_{cjy} v_{jx} \right|, \tag{24}$$

where n_a is the number of atoms located within the annular region, $\hat{r}_{cj}$ is the unit vector pointing from the center of the perturbed triangle to the center of atom j, $\vec{v}_j$ is the displacement vector of atom j, and $C = \sum_{j=1}^{n_a} |\vec{v}_j|$. We define the average "flux" of the displacement vectors through the annular region as

$$\Phi = \frac{1}{C} \left| \sum_{j=1}^{n_a} \hat{r}_{cj} \cdot \vec{v}_j \right|. \tag{25}$$

To characterize dipolar- and quadrupolar-like displacement fields, we measure the weighted local bond-orientational order parameters,[56]

$$\psi_k = \left| \sum_{j=1}^{n_a} \frac{s_j}{C} e^{ik\theta_j} \right|, \tag{26}$$

where $k = 2$ for dipolar and 4 for quadrupolar structures, θ_j is the angle between $\vec{v}_j$ and the x-axis, and $s_j = |\hat{r}_{cj} \cdot \vec{v}_j|$. For idealized (a) vortex, (b) point charge, (c) dipolar, and (d) quadrupolar fields, these definitions give the following values $(\Gamma, \Phi, \psi_2, \psi_4)$: (a) $(1,0,0,0)$, (b) $(0,1,0,0)$, (c) $(0,0.7,0.7,0.8)$, and (d) $(0,0,0,0.8)$. The idealized quadrupolar field is obtained from a single Eshelby circular inclusion with radius $4\sigma_{AA}$, Poisson's ratio $\nu = 0.343$, and 0.09 for the coefficient of the traceless eigenstrain[1] and the idealized dipolar field is obtained by weighting this quadrupolar field by $\cos^2\zeta$, where ζ is the angle between the quadrupolar field and one of the principal directions of the eigenstrain tensor of the Eshelby inclusion.

Acknowledgements

Notes and references

1   R. Dasgupta, H. G. E. Hentschel and I. Procaccia, *Physical Review Letters*, 2012, **109**, 255502.

2   R. Dasgupta, O. Gendelman, P. Mishra, I. Procaccia and C. A. Shor, *Physical Review E*, 2013, **88**, 032401.

3   R. Maaß and J. F. Löffler, *Advanced Functional Materials*, 2015, **25**, 2353–2368.

4   D. Şopu, A. Stukowski, M. Stoica and S. Scudino, *Physical Review Letters*, 2017, **119**, 195503.

5   R. J. Ivancic and R. A. Riggleman, *Soft Matter*, 2019, **15**, 4548–4561.

6   Y. He, P. Yi and M. L. Falk, *Physical Review Letters*, 2019, **122**, 035501.

7   F. R. N. Nabarro, *Theory of crystal dislocations*, Clarendon Press, Oxford, 1967.

8   A. Greer, Y. Cheng and E. Ma, *Materials Science and Engineering: R: Reports*, 2013, **74**, 71–132.

9   A. Argon, *Acta Metallurgica*, 1979, **27**, 47–58.

10 M. L. Falk and J. S. Langer, *Physical Review E*, 1998, **57**, 7192.

11 M. Zink, K. Samwer, W. Johnson and S. Mayr, *Physical Review B*, 2006, **73**, 172203.

12 F. Delogu, *Physical Review Letters*, 2008, **100**, 255901.

13 D. Richard, M. Ozawa, S. Patinet, E. Stanifer, B. Shang, S. Ridout, B. Xu, G. Zhang, P. Morse, J.-L. Barrat, L. Berthier, M. L. Falk, P. Guan, A. J. Liu, K. Martens, S. Sastry, D. Vandembroucq, E. Lerner and M. L. Manning, *Physical Review Materials*, 2020, **4**, 113609.

14 K. E. Avila, S. Küchemann, I. Alabd Alhafez and H. M. Urbassek, *Materials*, 2019, **12**, 1477.

15 F. Boioli, T. Albaret and D. Rodney, *Physical Review E*, 2017, **95**, 033005.

16 B. Xu, M. Falk, J. Li and L. Kong, *Physical Review B*, 2017, **95**, 144201.

17 J. Yu, A. Datye, Z. Chen, C. Zhou, O. E. Dagdeviren, J. Schroers and U. D. Schwarz, *Communications Materials*, 2021, **2**, 1–11.

18 G. Zhang, S. Ridout and A. J. Liu, *arXiv preprint arXiv:2009.11414*, 2020.

19 C. Maloney and A. Lemaitre, *Physical Review Letters*, 2004, **93**, 195501.

20 C. E. Maloney and A. Lemaitre, *Physical Review E*, 2006, **74**, 016118.

21 R. L. Jack, A. J. Dunleavy and C. P. Royall, *Physical Review Letters*, 2014, **113**, 095703.

22 J. M. Rieser, C. P. Goodrich, A. J. Liu and D. J. Durian, *Physical Review Letters*, 2016, **116**, 088001.

23 H. Tong and H. Tanaka, *Physical Review X*, 2018, **8**, 011041.

24 L. Gartner and E. Lerner, *Physical Review E*, 2016, **93**, 011001.

25 J. Zylberg, E. Lerner, Y. Bar-Sinai and E. Bouchbinder, *Proceedings of the National Academy of Sciences*, 2017, **114**, 7289–7294.

26 D. Richard, G. Kapteijns, J. A. Giannini, M. L. Manning and E. Lerner, *Physical Review Letters*, 2021, **126**, 015501.

27 J. Ding, S. Patinet, M. L. Falk, Y. Cheng and E. Ma, *Proceedings of the National Academy of Sciences*, 2014, **111**, 14052–14056.

28 S. Patinet, D. Vandembroucq and M. L. Falk, *Physical Review Letters*, 2016, **117**, 045501.

29 S. Patinet, A. Barbot, M. Lerbinger, D. Vandembroucq and A. Lemaître, *Physical Review Letters*, 2020, **124**, 205503.

30 Z. Fan and E. Ma, *Nature Communications*, 2021, **12**, 1–13.

31 M. L. Manning and A. J. Liu, *Physical Review Letters*, 2011, **107**, 108302.

32 J. Rottler, S. S. Schoenholz and A. J. Liu, *Physical Review E*, 2014, **89**, 042304.

33 C. Rainone, E. Bouchbinder and E. Lerner, *Proceedings of the National Academy of Sciences*, 2020, **117**, 5228–5234.

34 G. Kapteijns, D. Richard and E. Lerner, *Physical Review E*, 2020, **101**, 032130.

35 A. C. Lund and C. A. Schuh, *Applied Physics Letters*, 2003, **82**, 2017–2019.

36 H. Jónsson, G. Mills and K. W. Jacobsen, in *Classical and Quantum Dynamics in Condensed Phase Simulations*, ed. B. J. Berne, G. Ciccotti and D. F. Coker, World Scientific, Singapore, 1998, ch. 16, p. 385.

37 G. Henkelman, B. P. Uberuaga and H. Jónsson, *The Journal of*

Chemical Physics, 2000, **113**, 9901–9904.

38 G. Henkelman and H. Jónsson, *The Journal of Chemical Physics*, 2000, **113**, 9978–9985.

39 A. Nakano, *Computer Physics Communications*, 2008, **178**, 280–289.

40 E. Maras, O. Trushin, A. Stukowski, T. Ala-Nissila and H. Jonsson, *Computer Physics Communications*, 2016, **205**, 13–21.

41 C. Kittel, P. McEuen and P. McEuen, *Introduction to solid state physics*, Wiley, New York, 1976, vol. 8.

42 A. Takeuchi and A. Inoue, *Materials Transactions*, 2005, **46**, 2817–2829.

43 M. P. Allen and D. J. Tildesley, *Computer simulation of liquids*, Oxford University Press, Oxford, 1987.

44 S. Plimpton, *Journal of Computational Physics*, 1995, **117**, 1–19.

45 A. Tanguy, F. Leonforte and J.-L. Barrat, *The European Physical Journal E*, 2006, **20**, 355–364.

46 A. Barbot, M. Lerbinger, A. Hernandez-Garcia, R. García-García, M. L. Falk, D. Vandembroucq and S. Patinet, *Physical Review E*, 2018, **97**, 033001.

47 D. Klaumünzer, R. Maaß and J. F. Löffler, *Journal of Materials Research*, 2011, **26**, 1453–1463.

48 R. Ramachandramoorthy, J. Schwiedrzik, L. Petho, C. Guerra-Nunez, D. Frey, J.-M. Breguet and J. Michler, *Nano Letters*, 2019, **19**, 2350–2359.

49 R. Ramachandramoorthy, F. Yang, D. Casari, M. Stolpe, M. Jain, J. Schwiedrzik, J. Michler, J. J. Kruzic and J. P. Best, *Journal of Materials Research*, 2021, **36**, 2325–2336.

50 T. Albaret, A. Tanguy, F. Boioli and D. Rodney, *Physical Review E*, 2016, **93**, 053002.

51 W. G. Ellenbroek, Z. Zeravcic, W. van Saarloos and M. van Hecke, *EPL (Europhysics Letters)*, 2009, **87**, 34004.

52 P. Wang, S. Zhang, P. Tuckman, N. T. Ouellette, M. D. Shattuck and C. S. O'Hern, *Physical Review E*, 2021, **103**, 022902.

53 P. Schall, D. A. Weitz and F. Spaepen, *Science*, 2007, **318**, 1895–1899.

54 B. Utter and R. Behringer, *Physical Review Letters*, 2008, **100**, 208302.

55 E. D. Cubuk, R. J. S. Ivancic, S. S. Schoenholz, D. J. Strickland, A. Basu, Z. S. Davidson, J. Fontaine, J. L. Hor, Y.-R. Huang, Y. Jiang, N. C. Keim, K. D. Koshigan, J. A. L. Lefever, T. Liu, X.-G. Ma, D. J. Magagnosc, E. Morrow, C. P. Ortiz, J. M. Rieser, A. Shavit, T. Still, Y. Xu, Y. Zhang, K. N. Nordstrom, P. E. Arratia, R. W. Carpick, D. J. Durian, Z. Fakhraai, D. J. Jerolmack, D. Lee, J. Li, R. Riggleman, K. T. Turner, A. G. Yodh, D. S. Gianola and A. J. Liu, *Science*, 2017, **358**, 1033–1037.

56 D. R. Nelson and B. Halperin, *Physical Review B*, 1979, **19**, 2457.